nature communications

Article

https://doi.org/10.1038/s41467-025-60310-6

Design of circularly polarized phosphorescence materials guided by transfer learning

Received: 31 January 2025

Accepted: 19 May 2025

Published online: 29 May 2025

Check for updates

Xu Liu[1,3], Yihan Zhang[2,3], Yifan Xie[1,3], Ledu Wang[1], Liyu Gan[1], Jialei Li[1], Jiahe Li[1], Hongli Zhang[1], Linjiang Chen[1], Weiwei Shang[2] ✉, Jun Jiang[1] ✉ & Gang Zou[1] ✉

It is highly desirable that artificial circularly polarized phosphorescent materials with high luminescence asymmetry factor (g_{lum}), narrowband emission and tunable chiral phosphorescent performance can be constructed. Especially, precise control and simultaneous independent switching of circularly polarized fluorescent and phosphorescent performance for the same molecules remain a formidable challenge. Herein, we propose a strategy to customized design of circularly polarized phosphorescent materials based on large language models and transfer learning methods, which not only enables efficient identification of suitable synthesis precursors, but also provides valuable guidance for experimental procedures. We demonstrate the significant advantages of transfer learning with limited chemical data, and precisely fabricate films with high g_{lum} (1.86), narrow full-width at half-maximum (49 nm) and customized circularly polarized phosphorescent performance with targeted spectral position. The inverse customization of materials with user-specified circularly polarized fluorescent/phosphorescent performance can be achieved, favoring their application in multicolor display and multi-dimensional information encryption.

In recent years, circularly polarized phosphorescence (CPP) materials have garnered significant interest due to their unique properties including intrinsic chiroptical performance[1], long lifetime, large Stokes shift, and various potential applications in the field of 3D displays, anticounterfeiting and so on[2–6]. To date, a variety of CPP materials such as chiral inorganic materials[7], organic small molecules[8–11], self-assembling and polymer systems[12–14] have been developed and successfully employed in various chiroptical applications including sensing, displays, imaging and information encryption[15–17]. However, in most cases, the luminescence asymmetry factor (g_{lum}) of the reported CPP materials fall within the range of 10^{-3} to 10^{-2}, limiting their practical applications. To further amplify g_{lum} value, Prof. Deng et al. successfully doped chiral fluorescent helical polymer with chiral nematic liquid crystals to realize high g_{lum} of −1.87[18]. Similarly, Zhao and his colleagues developed a long-lived room-temperature phosphorescent system with a high g_{lum} of 1.49 based on polymer-stabilized cholesteric liquid crystals[19]. Extensive studies in this field are mainly focused on combining dye components with synthesis of chiral crystals or liquid crystal systems[20,21], but few reports have been described to achieve outstanding CPP performance in metal-free amorphous films[22]. Compared with the well-established technique using chiral molecules or assemblies[23,24], twisted stacking of multiple achiral anisotropic functional layers has become a popular method for fabricating chiral nanostructures with high g_{lum} values[25–28],which offers more

[1]State Key Laboratory of Precision and Intelligent Chemistry, School of Chemistry and Materials Science, University of Science and Technology of China, Hefei, Anhui, China. [2]State Key Laboratory of Precision and Intelligent Chemistry, Department of Automation, University of Science and Technology of China, Hefei, Anhui, China. [3]These authors contributed equally: Xu Liu, Yihan Zhang, Yifan Xie. ✉e-mail: wwshang@ustc.edu.cn; jiangj1@ustc.edu.cn; gangzou@ustc.edu.cn

freedom to regulate the chiroptical activity. In the previous studies, our group constructed a series of circularly polarized luminescence materials, in which g_{lum} can reach up to 1.9[29,30]. Different from fluorescent materials, phosphorescent molecules possess excellent photophysical behavior stemming from the transition from the triplet excitons to the ground state[31–33]. Therefore, combining circularly polarized fluorescent (CPL) and CPP properties into the same material and realize simultaneous modulation of CPP and CPL (with same or opposite handedness at targeted spectral position) is meaningful, as it can not only expand the freedom of chiral regulation but also integrate new functionalities for applications. However, most reported phosphorescent materials exhibit broad full-width at half-maximum (FWHM) and poor color purity. Additionally, due to the richness in design space for such twist-stacking structures, traditional experimental approaches based on trial-and-error are time-consuming and inefficient. Even in the simplest case, all design parameters must be simultaneously optimized, and the search-and-optimization process has to be repeated from beginning to end for every target chiroptical property (such as a certain g_{lum} value at a specific wavelength with a suitable FWHM). Meanwhile, the discovery process of synthesis precursors relies on researchers gathering information from the literature, which significantly slows down the development efficiency of new materials. Therefore, on-demand designing CPP materials with high g_{lum} value (>1), narrowband emission and customized CPP performance, especially from achiral amorphous films, remains a significant challenge.

Nowadays, data-driven machine learning (ML) techniques are rapidly gaining significant attention as a powerful and flexible approach to addressing the aforementioned issues. In previous studies, Professor Feng[34] and our group[29] demonstrated ML-based techniques to guide the synthesis of CPL materials with high g_{lum} values and multiple chiral regulation strategies. Typically, an ML model requires training on a substantial amount of data to effectively predict complex structure-property relationships; however, in many instances, the scarcity of high-quality data limits its application[35–37]. To tackle this challenge, transfer learning receives growing emphasis[38,39]. By pre-training models on similar tasks with larger datasets and subsequently fine-tuning them for target tasks, transfer learning effectively decreases the need for extensive data[40,41]. Yamada et al. developed a pre-trained model library that enables high-performance predictions of chemical properties under conditions of limited data[42]. In addition, the powerful text comprehension capabilities of generative language models position them as promising tools for chemical text mining[43]. With the availability of large-scale materials synthesis literature, large language models (LLMs) can now be used to recommend synthesis precursors for new target materials[44,45]. It is worth noting that combining LLMs with transfer learning methods can provide valuable guidance for the selection of suitable phosphorescent molecules and the construction of the chiral layer. The on-demand inverse design of CPP films with high g_{lum} values, narrowband emission and customized CPP performance guided by this integrated approach with limited chemical data, has not yet been described to date.

In this work, a strategy is utilized to guide the on-demand customization of CPP films based on LLMs and transfer learning (as shown in Fig. 1). Firstly, an LLM is used to search for phosphorescent molecules for the preparation of CPP materials (Fig. 1a). More than 500 articles on phosphorescent materials are processed by an embedding model to build a vector database of literature texts, which is later referenced by an LLM via the Retrieval Augmented Generation (RAG) method to generate a summary of molecules and properties of each article using prompt words, the LLM is used to summarize and screen the text to generate a list of molecules that met the requirements. Here, three phosphorescent molecules are selected manually from the list. Secondly, to build the relationship between structure and function of the CPP materials, machine learning has been introduced (Fig. 1b). Given the complexity of the twisted-stacking structure and the richness in design space, constructing a relationship between structure/process parameters and target CPP performance poses a challenge. Therefore, transfer learning is utilized to construct the structure-function relationship, which facilitates accurate forward prediction of CPP performance from experimental phosphorescent spectra and structure/process parameters. Finally, inverse design and customized

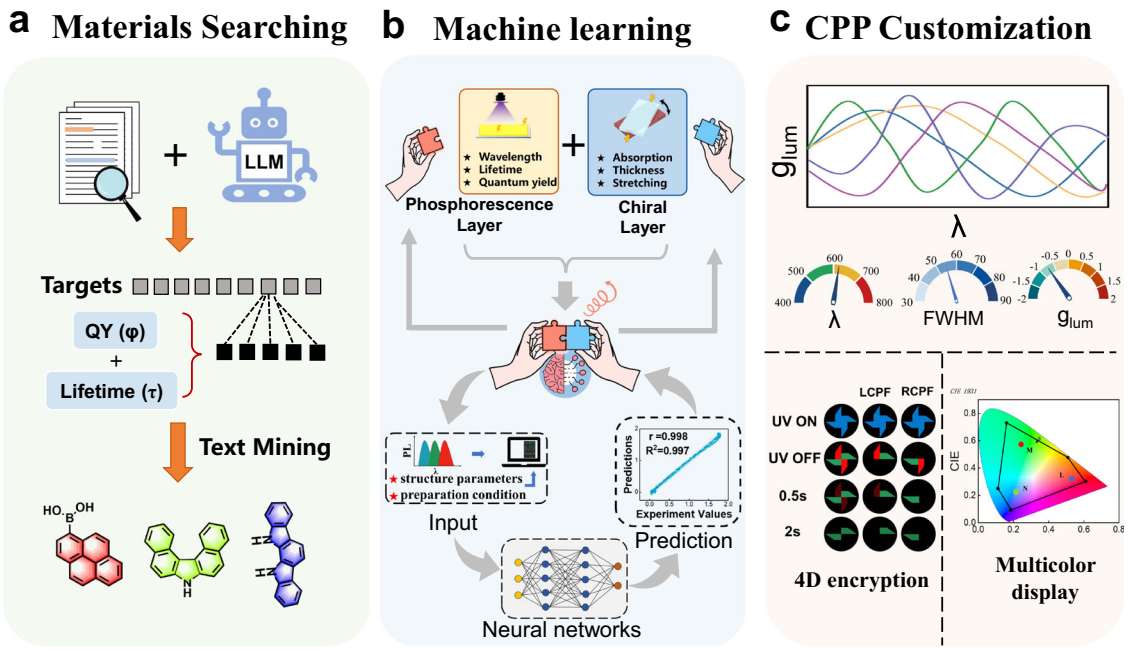

Fig. 1 | The on-demand customization of CPP films with target functionality guided by LLMs and transfer learning. a Recommendation of target materials with LLMs. **b** Construction of the structure-spectrum-function relationship based on transfer learning. **c** Inverse design and customized manufacturing of CPP films with target functionality.

https://doi.org/10.1038/s41467-025-60310-6

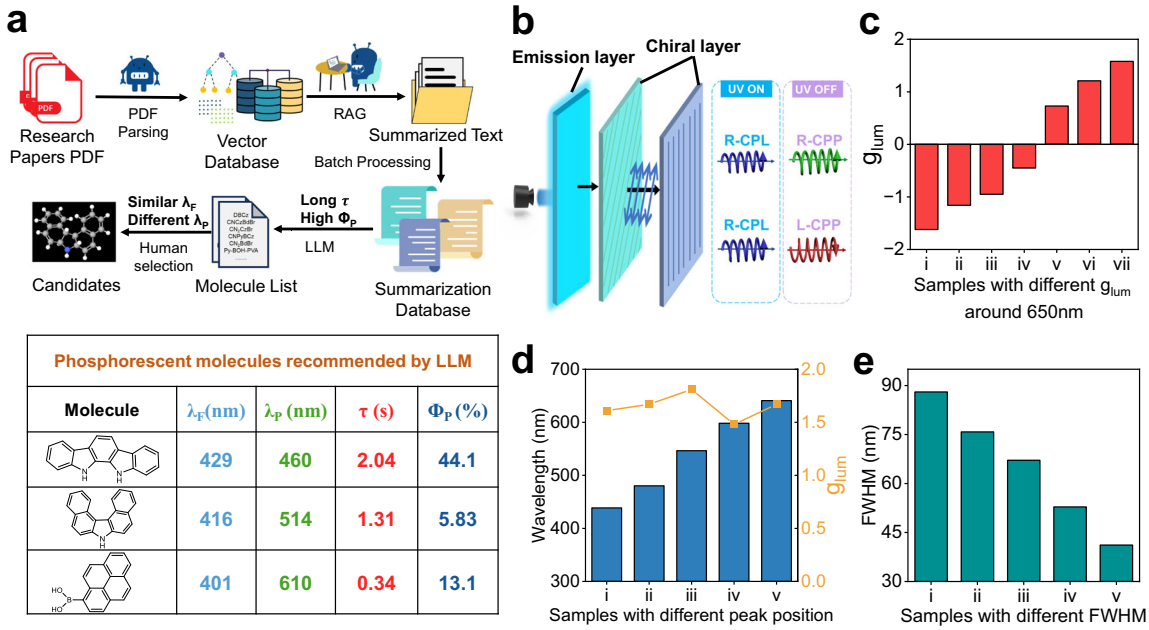

Phosphorescent molecules recommended by LLM

Molecule	λ_F(nm)	λ_P (nm)	τ (s)	Φ_P (%)
	429	460	2.04	44.1
	416	514	1.31	5.83
	401	610	0.34	13.1

Fig. 2 | LLMs recommendation and CPP performance of the hybrid films. **a** Flowchart of molecular recommendation by LLMs. **b** Schematic illustration of the generation of CPP through the twisted stacking structure. CPP performance of the samples with (**c**) different g_{lum} values at around 650 nm by adjusting the thickness and strain of transparent oriented PVA layer. **d** Different peak position but similar g_{lum} values by varying the strain of transparent oriented PVA layer and the dye molecules. **e** Different FWHM by varying the combinations of the thickness and strain of transparent oriented PVA layer as well as the dye molecules.

manufacturing of CPP films with target functionality can be achieved (Fig. 1c). We demonstrate the significant advantages of transfer learning with limited chemical data, which can guide the precise fabrication of chiral phosphorescent films with high g_{lum} up to 1.86, narrow FWHM of 49 nm and customized CPP performance with the targeted spectral position across the full visible spectrum. Moreover, the proposed inverse design enables flexible switching of phosphorescent color with high purity of 95% for multicolor display and customization of both CPL and CPP performance (with the same or opposite handedness at targeted spectral position) from the same phosphorescent molecules, which provides a dimension for information encryption. It is anticipated that these findings not only provide the customization design of CPP materials but also are of great fundamental value for underscoring the promise of ML-driven design approaches in the development of functional materials.

Results

LLMs for precursor selection and CPP performance regulation

In the preparation of CPP materials with high g_{lum} values, high quantum efficiency and long lifetime, phosphorescent molecule selection plays a crucial role in governing the preparation pathway. To extract the complex and diverse information embedded in chemical literature, LLM was used to choose suitable phosphorescent molecules (Fig. 2a). We collected over 500 documents on the design and discovery of phosphorescent materials, downloaded them as PDF files and processed them into vector databases using LangChain. Utilizing RAG technology, we summarized the textual information and compiled these summaries into a database. This approach processes scientific articles in their entirety. It creates vector embeddings of textual content (paragraphs), then retrieves relevant information based on the semantic similarity of the text, and augments the LLM's generation with this contextually relevant information. Furthermore, we enabled Long Context mode in LLMs to maintain a detailed record of extended textual content, thus facilitating the processing and generation of complex data sets. Our system processes chemical information as it naturally appears within scientific literature. The LLM processes this information contextually, including any SMILES strings, chemical formulas, or descriptive text about molecular properties that might be present in the retrieved passages. This approach allows for a more natural and comprehensive handling of chemical information within the framework of scientific knowledge (Supplementary Fig. 1). To focus our study, we applied constraints such as room-temperature, long lifetime, and high quantum efficiency, leading to a list of phosphorescent molecules generated by the LLM (Supplementary Table 1). From this list, we manually selected three molecules: 1-pyrenylboronic acid (PA), 7H-dibenzo[c,g]-carbazole (DBCz), and 11,12-dihydroindolo[2,3-a]carbazole (ICz). These molecules all exhibited similar blue fluorescence emissions, but different phosphorescence emissions, including blue for ICz, green for DBCz and red for PA, when they were compounded with polyvinyl alcohol (PVA), respectively (Fig. 2a and Supplementary Figs. 2–4). All chiroptical films were prepared by overlaying one transparent oriented PVA layer (as a phase retarder) onto another highly oriented dyed PVA layer (as a polarizer with selective absorption) in a twisted fashion to fabricate a twisted stacking structure[30]. Large optical activities can be observed when the twist angle is ±45° (Supplementary Fig. 5), in accordance with the prediction based on Jones Matrix mechanism[46]. There are several variable parameters, including the thickness and stretching degree of the transparent oriented PVA layer, greyscale and dye molecules selection of highly oriented dyed films as well as the twist angle, which greatly affect their optical activities (Supplementary Figs. 6–9). Then, CPP materials can be obtained by integrating isotropic phosphorescent molecules/PVA hybrid films with above twisted stacking structure films (Fig. 2b). Their CPL and CPP performance could be defined by asymmetry factor g_{lum} ($g_{lum} = 2(I_L\text{-}I_R)/(I_L + I_R)$), where I_L and I_R were the emissions of left-handed and right-handed circularly polarized light. The generation of CPL and CPP could be understood based on a Muller matrix for a combination of polarizer and phase retarder[25]. The linearly polarized fluorescence (phosphorescence) would be produced after passing through the highly oriented dyed PVA layer (as the polarizer), and then CPP would be produced after passing through the transparent oriented PVA layer (as a phase retarder) in a twisted fashion (Fig. 2b). In total more than 10^8 possible combinations are estimated to achieve different CPP performance. Flexibly manipulating the CPP

https://doi.org/10.1038/s41467-025-60310-6

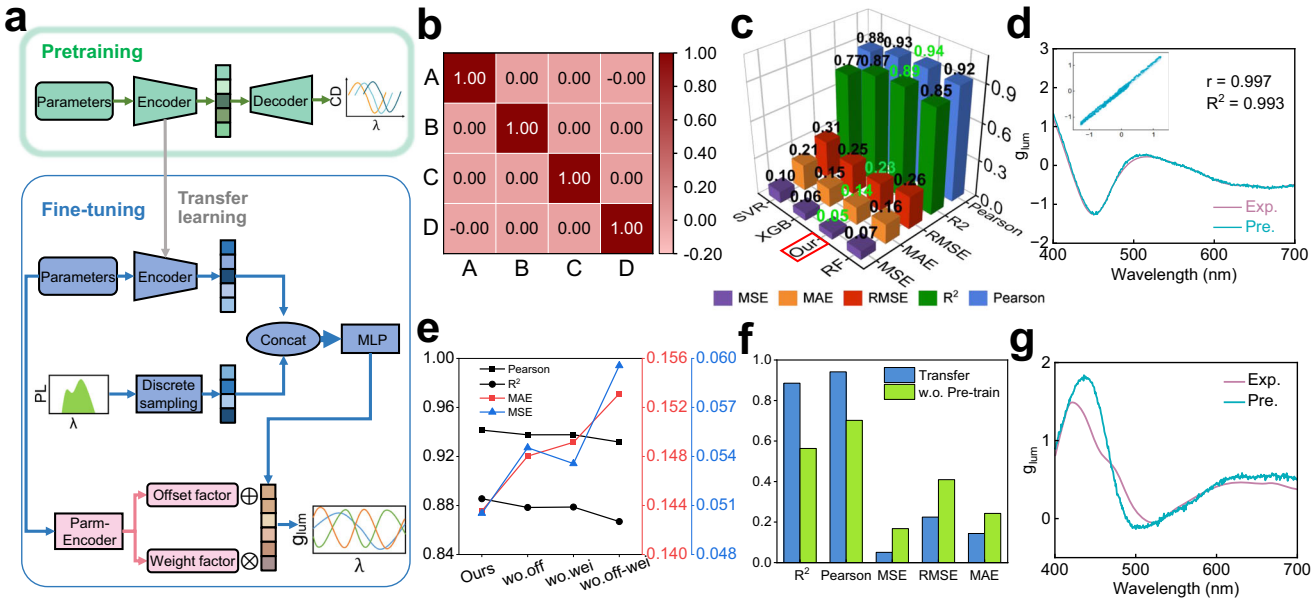

Fig. 3 | Transfer learning framework and forward prediction results. a The framework of transfer learning. **b** Correlation heat map of the features. **c** Mean square error, mean absolute error, root mean square error, coefficient of determination and Pearson correlation coefficient histogram of the models. **d** Fitting curves of experimental and predicted results. **e** The curve of MSE, MAE, RMSE, R^2 and Pearson correlation coefficient for models with different encoding factors. **f** Histogram of mean square error, mean absolute error, root mean square error, coefficient of determination and Pearson correlation coefficient for models with and without pretraining. **g** Zero-shot generalization of forward prediction model.

performance in a simple way always remains challenging[15]. By altering the above variable structure/processing parameters and their combinations, a continuous modulation of CPP performance including the sign, magnitude, peak position as well as FWHM could be achieved (Fig. 2c–e and Supplementary Figs. 10–12).

Transfer learning model for forward prediction

Due to the richness of design space, precise forward prediction of the CPP performance of the hybrid films based on traditional trial-and-error approaches seemed unlikely, since these variable parameters often correlated with each other. In our previous work, we established a quantitative structure-spectrum-function relationship between the structural parameters, spectral features and circular dichroism (CD) properties of the twisted stacking structure, and realized precise forward prediction based on machine learning techniques[29]. Herein, the CD dataset of the twisted-stacking structures in our previous work was recruited to solve this problem. Predicting the CD spectra was adapted as a pre-training task for assisting the prediction of g_{lum} for CPP materials. To further enhance the accuracy of the forward prediction model, 135 combinations of parameters were employed to construct CPP hybrid films, and their CPL as well as CPP performance was measured. The fluorescence spectrometer was used to measure the emission spectra of the composite film in the presence of left-handed and right-handed circular polarizers. Then, according to the formula $CPL = I_L - I_R$, the circular polarized luminescent properties of the composite film were obtained. Furthermore, based on the formula $g_{lum} = 2(I_L\text{-}I_R)/(I_L + I_R)$, the spectrum of g_{lum} varying with the wavelength was calculated, which was used as the data source for model training (Supplementary Figs. 13–15). This dataset was used for both training and validation of the forward prediction model. To efficiently simulate the g_{lum} spectra properties of the CPP materials, a forward prediction model based on transfer learning has been developed. Given the spectroscopic properties of g_{lum}, the forward prediction neural network was modeled as a multivariate regression problem. As shown in Fig. 3a, the model input consisted of two components: one was the spectral embedding descriptor, which included various structural and process parameters such as thickness, the stretching degree, grayscale, twist angle, and dye absorption. The composition of the spectral embedding descriptor vector is detailed in Supplementary Table 2. The other input is the emission spectrum of the phosphorescent molecule, exhibiting a wavelength range spanning from 400 to 700 nm and a data interval set at 0.2 nm. To illustrate the validity of the selected structural and process parameters, we analyzed the correlation among the four features using a correlation coefficient heatmap. The four elements in Fig. 3b represent the types of polarization layer dyes and phosphorescent molecules, the thickness of the phase delay layer, and the stretching degree of the phase delay layer, respectively. While the non-primary diagonal elements in the figure are close to 0, indicating that there is no linear correlation between the variables A, B, C, and D. The results indicated that these variables were completely independent of each other, which further validated the balance and effectiveness of the dataset (Fig. 3b). During the pre-training phase, an encoder-decoder architectural framework was utilized to map the structural and process parameters of the film into an embedding space, subsequent to which the embedded information was decoded for the generation of CD spectra. The latent representations in the embedding space were extracted, implicitly containing information on the absorption properties of chiral films, facilitating knowledge transfer and supporting the subsequent integrated modeling of g_{lum} spectra. In the fine-tuning phase, the model used the pre-trained encoder to generate latent features. These latent features were concatenated with the phosphorescent molecular emission spectra and fed into a Multi-Layer Perceptron (MLP), which output a reference vector **x** of the same dimension as the g_{lum} spectrum. Considering the different modulation mechanisms of process/structural parameters on the g_{lum} spectrum, a parameter encoder was also designed to encode the process/structural parameters into offset factor **β** and weight factor α. The implementation details of the parameter encoder were introduced in the Method-Model Architecture section. Using these two factors, the reference vector **x** was further adjusted to generate the

https://doi.org/10.1038/s41467-025-60310-6

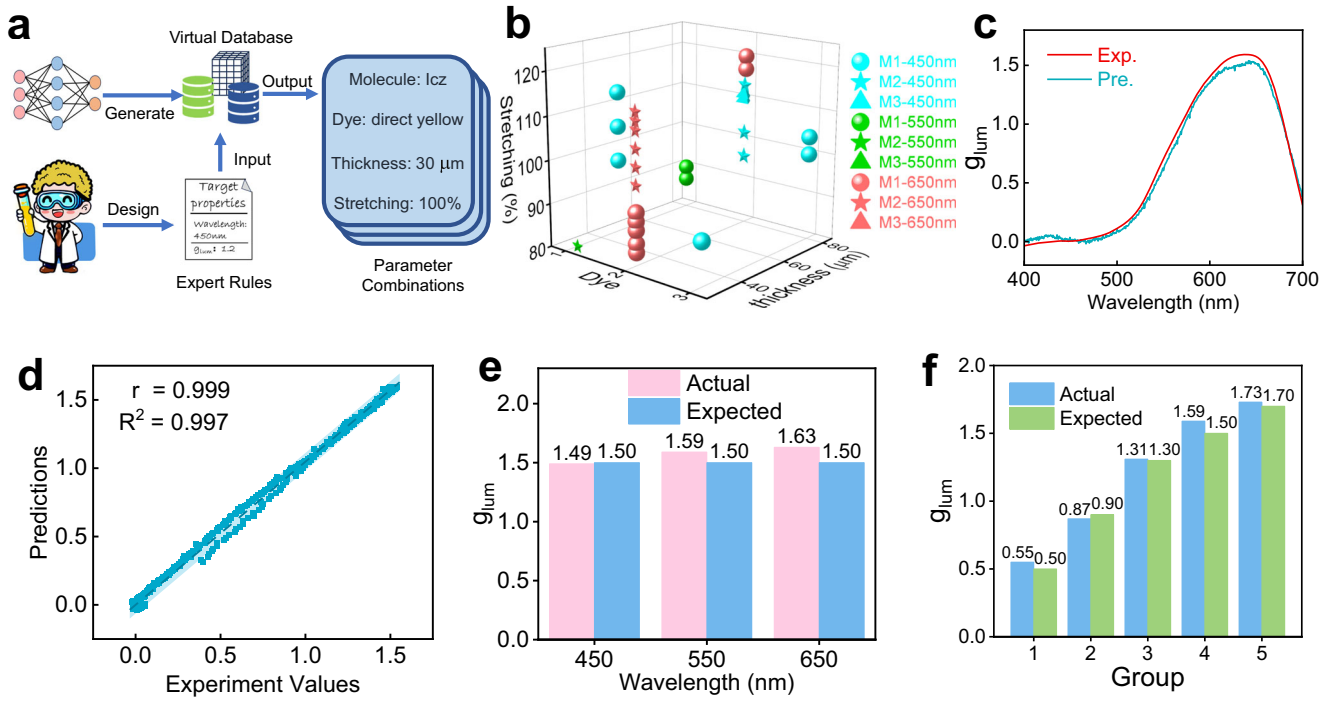

Fig. 4 | Reverse model for inverse design of CPP materials. a Schematic diagram for the inverse design. **b** Parameters generated by inverse design. **c** Fitting curves and **d** scatter plots of experimental and predicted results. Actual values and expected values histograms for the samples of experimental realization using inverse design for the targets: **e** g_{lum} = 1.5 at 450 nm, 550 nm, 650 nm; and **f** g_{lum} = 0.5, 0.9, 1.3, 1.5, 1.7 at around 550 nm, respectively.

final prediction result $\boldsymbol{\lambda}$, as expressed in the following equation:

$$\boldsymbol{\lambda} = \alpha \cdot (\mathbf{x} + \boldsymbol{\beta}) \tag{1}$$

We established a model evaluation scheme with 10-fold cross-validation and employed five evaluation metrics to assess the model performance, including mean square error (MSE), mean absolute error (MAE), root mean square error (RMSE), coefficient of determination (R^2) and Pearson correlation coefficient (Pearson). For different models, higher MSE, MAE, and RMSE values indicate worse model performance, while higher R^2 and Pearson values reflect better performance. We comparatively analyzed our model with several other machine learning regression models including Random Forest (RF), Support Vector Regression (SVR), and XGBoost algorithms. Our model demonstrated the best predictive performance, with the lowest MAE of 0.14 and the highest R^2 of 0.89. Furthermore, our model exhibited a relatively lower standard deviation in the predicted results, indicating its superior consistency and stability (Fig. 3c and Supplementary Table 3). Figure 3d visualizes the g_{lum} predictions of a test sample against experimental fittings, showcasing the model's prediction capability. The predicted curve closely aligns with the experimental curve, achieving an excellent R^2 of 0.993. The points in the scatter plot predominantly follow the line of $y = x$, suggesting a strong consistency between the predicted and experimental values. Additionally, to evaluate the effectiveness of the parameter encoder and transfer learning, ablation experiments were designed to compare performance differences with the absence of various components. Compared to models missing the offset factor, weight factor, or both, the original complete parameter encoding resulted in better predictive performance, indicating that both encoding factors contribute to more effective learning of the structure-spectrum-function relationship (Fig. 3e and Supplementary Table 4). To demonstrate the necessity of adopting transfer learning, we compared our model with the model without transfer learning. The result showed our approach significantly improved prediction accuracy. The MAE decreased from 0.24 to 0.14 (Fig. 3f and Supplementary Table 5), demonstrating that the material latent representations extracted via transfer learning effectively capture the absorption characteristics of the film materials. In order to further illustrate the predicted effect of our model and its practical application value, we also explored the model's zero-shot regression capability. We prepared CPP materials in which methyl orange was used for the dye layer in the chiral film and our model had not been trained on experimental data for this dye. The robustness and generalization potential of the method was demonstrated by comparing the curves given by the model with the curves obtained from the experiments (Fig. 3g). As a polarized dye present in a pre-trained database, it is possible to predict the g_{lum} spectrum of the CPP material made from this dye, even if the model has not been trained on related data.

Inverse design of CPP materials

The established structure-spectrum-function relationship of CPP materials based on transfer learning can be further exploited in an inverse model for personalized customization of CPP materials with target functionality. Utilizing a forward prediction model, a virtual database was established, containing various predefined structural parameter combinations and their corresponding g_{lum} spectra, generated by the forward model. Therefore, the predefined structural parameter combinations expanded the existing dataset of 135 samples, which includes all possible combinations of 41 different stretching degrees (ranging from 80% to 120%) and other parameters within original ranges, totaling 1,107 data points. Researchers can formulate structural expert rules based on specific experimental scenarios and retrieve data from the virtual database according to these rules. After comparison and selection, the system will generate all possible structural parameter combinations that meet the required criteria, and the inverse design system was established, as outlined in Fig. 4a. The target CPP performance is user-defined and can take any form expressible from the CPP spectral features, e.g., a certain g_{lum} value (1.5) at a certain wavelength (450 nm, 550 nm, and 650 nm, respectively). Upon

https://doi.org/10.1038/s41467-025-60310-6

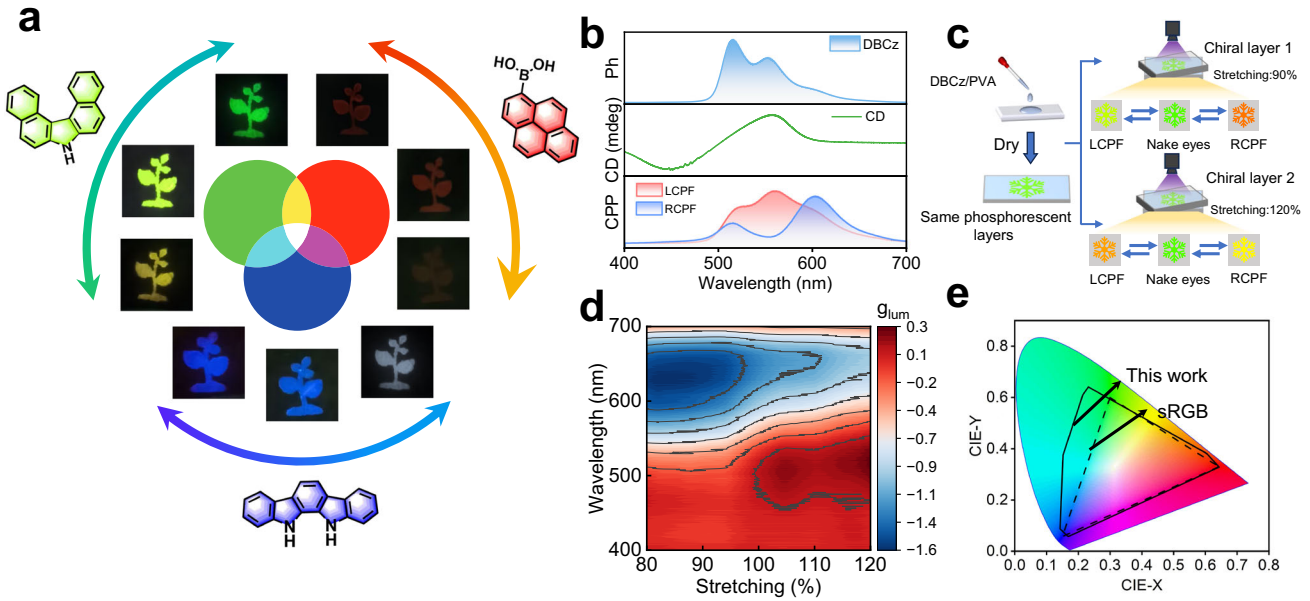

Fig. 5 | CPP materials towards circular polarization-based multicolor display. **a** Schematic diagram for the CPP materials with controllable color switching performance in phosphorescent emission. **b** The phosphorescence (Ph), CD and circularly polarized phosphorescent (CPP) spectra of the DBCz/PVA hybrid chiral films. **c** Different color switching performance could be achieved by only varying the stretching degree of PVA layers (90% and 120%, respectively). **d** The influence of stretching on the g_{lum} value of the hybrid films. The data is sourced from a virtual database, which was generated under the following conditions: the phosphorescent molecule is DBCz, the dye of the polarization layer is Direct Blue 71, the thickness of the phase retardation layer is 48 μm, and the stretching degree of the phase retardation layer is varied from 80% to 120%. The interval of the stretching degree between each group of data is 1. **e** Color gamut of the CPP materials in CIE1931 chromaticity diagram. A typical sRGB color gamut is shown for comparison.

inputting the target g_{lum} value and corresponding wavelength into the inverse design system, a set of structure/process parameters combinations and phosphorescent molecule selections was generated, as shown in Fig. 4b. There are typically many available answers for a given target, since the hybrid films with different phosphorescent molecules and various structure/process parameters combinations would exhibit the same g_{lum} value at a certain wavelength. To evaluate the accuracy of the inverse design system, one of the possible parameters combinations was chosen to experimentally construct the hybrid film. As shown in Fig. 4c and 4d, the experimentally measured g_{lum} spectra matched well with the predicted spectra and most of the data points in the scatter plot align closely with the $y = x$ line, with an R^2 value of 0.997, indicating its excellent accuracy. Figure 4e contains a histogram for the inversely designed and as-prepared films that can generate g_{lum} value of 1.5 at 450 nm, 550 nm, and 650 nm, respectively. The output of the inverse design system always consistently satisfies the specified design requirements (Supplementary Fig. 16), with errors maintained below 10%. Moreover, when a series of g_{lum} values (0.5, 0.9, 1.3, 1.5, and 1.7) at a certain wavelength (e.g. around 550 nm) were needed, the inverse design system can successfully report a set of possible selections of phosphorescent molecules and structure/process parameters combinations. Compared with the predicted spectra, the experimentally measured g_{lum} spectra exhibited excellent accuracy (Fig. 4f and Supplementary Fig. 17), confirming the success of our inverse design system for CPP films with target g_{lum} value at a certain wavelength.

Inverse design of multicolor display

The successful achievement of the inverse design system in precise prediction of single g_{lum} values at a single wavelength for CPP materials inspired us to extend our method to multiple g_{lum} values at multiple wavelengths, to meet the demand of multicolor display. As illustrated in Fig. 5a, the resultant CPP color depended not only on the selection of phosphorescent molecules but also on the constitution of the hybrid films. Taking DBCz as an example, in the absence of the chiral layer, the DBCz/PVA hybrid films exhibited green broad bandwidth phosphorescent emission, as depicted in Fig. 5b and 5c. Overlaying a transparent oriented PVA layer (the stretching degree of 90% as a phase retarder) onto another highly oriented Congo Red dyed PVA layer (as a polarizer) was utilized to fabricate a twisted stacking chiral layer. It should be noted here that the formed chiral layer exhibited giant optical activity and frequency selective transmission, which can be exploited as a circular polarization-based filter (CPF) for multiplex color switching. As expected, two different phosphorescent spectra could be obtained through L- or R-CPF, respectively (Fig. 5b). Thus, a green-cyan color switching in phosphorescent emission could be observed when viewed through L-CPF. Similarly, green-reddish orange color switching in phosphorescent emission could be observed when viewed through R-CPF (Fig. 5c, chiral layer 1). As mentioned above, the effective phosphorescent color switching greatly depended on their giant optical activity and frequency selective absorption properties of the chiral layer. Interestingly, by only varying the stretching degree of the transparent PVA layer (e.g. 120%), the chiral layer exhibited corresponding red shift in CD characterizations (Supplementary Fig. 18). Therefore, different color switching in phosphorescent emission could be observed when viewed through L- or R-CPF, respectively (Fig. 5c chiral layer 2, and Supplementary Fig. 19). Notably, only increasing the stretching degree of the PVA layer induces an overall red shift in the g_{lum} spectrum (Fig. 5d and Supplementary Fig. 20), greatly enhancing its effective color switching range in phosphorescent emission. Each of the three different constitutions of the hybrid films (including ICz, DBCz and PA) could work as a phosphorescent emission switch among three prime colors. Together, these three systems constitute a circular polarization-based full-color phosphorescent display. Any color within the enclosed area in the CIE1931 chromaticity diagram could be achieved and further switched based on above inverse design model for selecting suitable phosphorescent molecules and structure/process parameters combinations. This color space covers ~145% of a typical sRGB color gamut found in commercial color displays (Fig. 5e). For comparison, the color gamut of our previous system without the help of inverse design only reached 67% of the sRGB. Furthermore, our

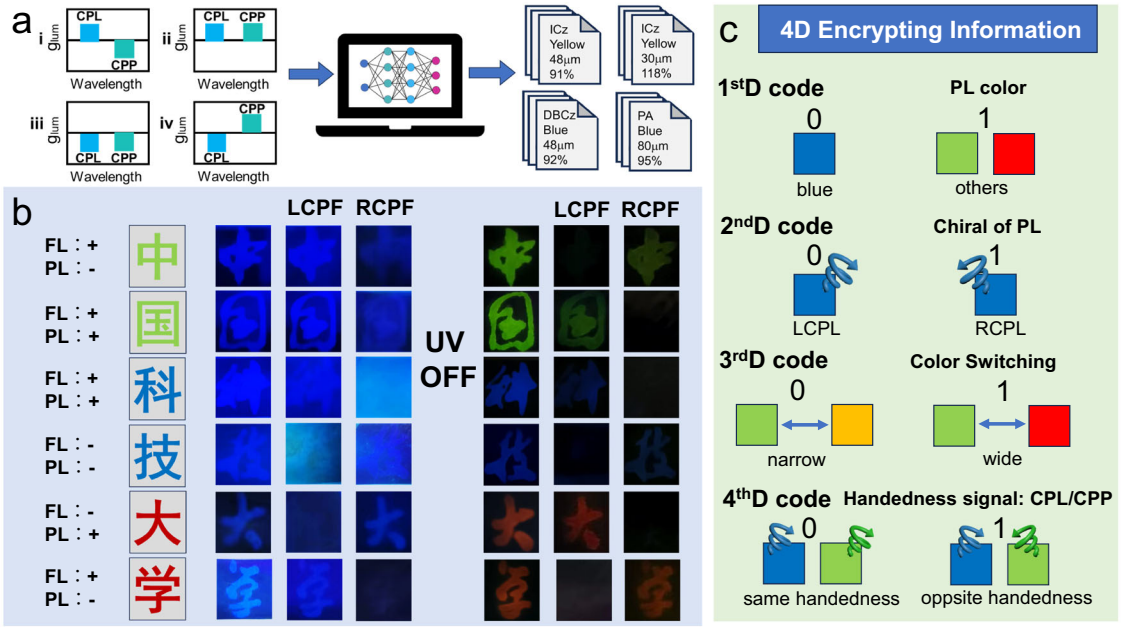

Fig. 6 | Inverse design and 4D information encryption. a Schematic diagram for the inverse design of CPP films with programmable CPL and CPP performance and **b** their fluorescence and phosphorescence images viewed with naked eyes, through L- or R-CPF, respectively. **c** Encoding terminology of 4D information encryption and decryption.

method effectively narrows the full-width at half maximum (FWHM) of the emission spectra of the phosphorescent materials, which can be utilized to enhance the emission color purity. For instance, for DBCz/PVA, by selecting a chiral layer with Congo Red dye, thickness of 80 μm, and stretching degree of 110%, the color purity was increased to about 95%, with the corresponding CIE coordinates being (0.480, 0.503) (Supplementary Fig. 21).

Inverse design of 4D encrypting information

It would be highly desirable to design and controllably synthesize CPP materials with programmable CPL and CPP performance, e.g. with the same or opposite handedness, which could serve as unique photonic components in chiral optoelectronics and nanophotonics. However, the customized manufacturing of CPP materials with tailorable CPL and CPP properties would be very difficult based on traditional techniques such as the utilization of chiral dopants or chiral liquid crystals. But the success of inverse design for the chiral layer with multiple g_{abs} values at multiple wavelengths allows us to easily customize programmable CPL and CPP performance from the same phosphorescent layer. As shown in Fig. 6a, the target function was user defined (CPL and CPP performance with the same or opposite handedness) and was input into the computational brain, which could be processed with the inverse design model and a set of structure/processing parameters that approaches the target function were reported. For example, we defined left-handed blue CPL but right-handed green CPP as the target function, which was input into the inverse design model, and the suitable structure/processing parameters were given (Supplementary Fig. 22). As expected, only blue CPL "中" image could be viewed through L-CPF, while green CPP "中" image could be viewed through R-CPF, indicating that the produced sample exhibited the customized CPL and CPP performance with opposite handedness (Fig. 6b). Interestingly, we defined right-handed blue CPL and green CPP as the target function, and the sample could be successfully fabricated with right-handed blue CPL and green CPP performance based on the inverse design model. Similarly, the target function with same handed blue CPL and CPP or opposite handed blue CPL and red CPP performance could be realized successfully (Supplementary Figs. 23 and 24), experimentally demonstrating the excellent accuracy of our inverse design model. All above results indicated the successful customization of programmable CPL and CPP performance at multiple predesigned wavelengths.

Further, we attempted to combine their programmable CPL and CPP characteristics to achieve 4D information encryption. As shown in Fig. 6c, the color of the phosphorescence emission is used as the first dimensional code (1stD code). The blue phosphorescent emission represents '0', while others represent '1'. The handedness of the CPP could be used as the second dimensional code. The left-handed CPP represents '0', while right-handed CPP represents '1'. As mentioned above, different color switching in phosphorescent emission could be observed through L- or R-CPF, respectively. By varying only the stretching degree of the PVA layer, different color switching range in phosphorescent emission could be achieved even from the same phosphorescent layer. Similarly, programmable CPL and CPP properties with same or opposite handedness could also be achieved from the same phosphorescent layer. Consequently, the effective color switching in phosphorescence emission and programmable CPL and CPP properties could be used as two other dimensions of encryption (Fig. 6c). Such a 4D bar code is much more complex than the other traditional system using only color, lifetime and chirality as the dimensions of encryption. Taking advantage of the above multi-mode characteristics of our 4D information encryption system, the information capacity and security would be greatly enhanced, holding significant potential applications for safeguarding valuable and authentic information.

Discussion

In summary, we demonstrated a workflow for the on-demand customization of functional materials with programmable CPL and CPP performance based on LLMs and transfer learning methods. The relationship between the structure of functional materials and their CPL and CPP performance has been built, allowing us to not only facilitate accurate forward prediction of CPP performance from experimental structure/process parameters, but also provide valuable guidance for personalized customization of CPP materials with target functionality. We demonstrate the significant advantages of transfer learning with limited chemical data, and facilitate the precise

fabrication of CPP films with high g_{lum} up to 1.86, narrow full-width at half-maximum (FWHM, 49 nm) and customize CPP performance with targeted spectral position across the full visible spectrum. As a result, the on-demand customized CPP materials were exploited to fabricate programmable chiroptical components towards multiple practical applications including multicolor display and 4D multi-mode information encryption.

It is anticipated that these findings will not only shed light on the inverse design of chiroptical materials and devices with target functionalities, but also is of great fundamental value for discovering and optimizing functional materials for cutting-edge applications based on ML-driven method.

Methods

Materials and instruments

All chemicals were used without further purification. PVA (Mw:445000 g/mol), Direct Blue 71, Direct Yellow, and Congo Red dyes were purchased from Aladdin. The PVA films (30 μm, 48 μm, 80 μm) were purchased from New Blue Sky Materials Industry Co., Ltd. 7H-dibenzo[c,g]-carbazole (DBCz), 11,12-dihydroindolo[2,3-a]carbazole (ICz) and 1-pyrenylboronic acid (PA) were purchased from Aladdin, respectively. The DBCz/PVA, ICz/PVA and PA /PVA hybrid phosphorescent films were separately prepared upon drop casting method[47–49]. Chiral films with twisted-stacking structure were constructed by a modified method in analogy to the previous procedure[29]. The top transparent highly stretched PVA layer acts as a phase retarder, while the bottom stretched dyed PVA layer (with Direct Blue 71, Congo Red and Direct Yellow, respectively) serves as a polarizer. The stretching degree γ of PVA layer was characterized as the ratio between the increased length and the original length upon stretching. The bottom dyed PVA layer was rotated in either a clockwise or counter-clockwise fashion with respect to the top layer to generate chiroptical performance. Then the combination of above phosphorescent film and chiral films could generate both CPL and CPP performance.

Characterization

UV-vis absorption spectra were measured by a Shimadzu UV-2700. The fluorescence spectrum was obtained by a fluorescence spectrometer (SHIMADZU RF-6000), while phosphorescence luminescence spectrum was obtained by other fluorescence spectrometer (Hitachi F-4700). The asymmetry factor of luminescence was calculated based on $g_{lum} = 2\times(I_L\text{-}I_R)/(I_L + I_R)$ (the detail was described in Supplementary Fig. 25). In order to verify the correctness of the method, circular polarized photoluminescence was directly measured using a JASCO CPL-300 spectrometer. CD characterization was performed by a commercial CD spectrometer (JASCO-1500). Photographs were captured using a Redmi K50 smartphone under UV lamp illumination at room temperature.

Dataset

The dataset used for pre-training contains 1,493 samples, all of which were collected by our group in previous work[29]. Each sample includes four structural/process parameters, the selective absorption of dye molecules, and the corresponding CD spectra of the material.

The Fine-tuning dataset contains two sets of samples, each consisting of 135 samples. The input information for each sample includes the phosphorescent and fluorescence luminescence spectra of phosphorescent molecules (corresponding to the two groups of samples), the selective absorption of dye molecules, and four structural parameters. Specifically, three luminescent molecules, three dye molecules (Direct Blue 71, Direct Yellow, Congo Red), three film thicknesses (30 μm, 48 μm, 80 μm), five stretching degrees (80%, 90%, 100%, 110%, 120%), one grayscale, and one twist angle were selected. Each set of samples was fully sampled for all possible combinations. Correspondingly, the output of each sample is the g_{lum} spectrum of the CPP material fabricated under the given input parameter combination.

Model architecture

Forward prediction model includes two key components: pre-training task and parameter-encoder. In the pre-training task, the encoder employs a 5-layer MLP, while the decoder utilizes a 1-layer MLP.

The parameter encoder selectively encodes input features, to generate the offset factor ($\boldsymbol{\beta}$) and the weight factor (α). These factors are implemented using MLPs and trainable embeddings. In particular, the offset-related features, which include thickness, dye species, and stretching properties, are first processed through a 3-layer MLP. The output is then modulated via element-wise multiplication with a learnable parameterized embedding to obtain the offset factor. Similarly, the weight-related feature, which is thickness, is processed through a dedicated 2-layer MLP to generate the weight factor. This factor is further constrained within the range [−1.5,1.5] to prevent excessive scaling effects. Since thickness and dye species are discrete variables, one-hot encoding is applied before processing.

All models were constructed and trained using the PyTorch framework. The forward prediction model consists of 5.56 M parameters, while the pre-trained autoencoder contains 0.41 M parameters. To expand the training dataset, Gaussian noise with a standard deviation of 1×10^{-7} was added to absorption properties of the dye before training, so that the dataset was extended tenfold.

Ablation study

The ablation study focuses on two key modules: transfer learning and the parameter encoder. Firstly, to verify the necessity and effectiveness of transfer learning, we examined the model's performance without the pre-training task. Specifically, the spectral embedding descriptors were concatenated with the emission spectra of phosphorescent molecules and directly fed into the MLP, bypassing the encoder-decoder structure. Additionally, in order to analyze the effectiveness and influence of the two factors from the parameter encoder, three model variants were designed: (1) excluding the weight factor α, (2) excluding the offset factor $\boldsymbol{\beta}$, and (3) excluding both. These three cases are where α equals [1], $\boldsymbol{\beta}$ equals [$\mathbf{0}$], and both α equals [1] and $\boldsymbol{\beta}$ equals [$\mathbf{0}$] together.

Hyperparameters setting

The hyperparameter batch_size is set to 128, the initial learning rate is 5×10^{-5}, and the attenuation rate is 0.7. The optimization algorithm used in the model is Adam, with training over 300 epochs. All training hyperparameters and model configuration details are provided in Supplementary Table 6. In addition, in order to make the most of the dataset and evaluate the overall performance of the model, 10-fold cross-validation was employed. As a result, all reported predictions are based on the entire dataset, without relying on single data split. Finally, five independent repeated experiments were set up and showed similar results.

Hardware setup and software environments

The experiments were conducted on a computing system equipped with an NVIDIA RTX 2080 Ti GPU (11GB VRAM) and a 12 vCPU Intel Xeon Platinum 8255 C CPU @ 2.50 GHz, supported by 40GB system memory. The software stack included CUDA 11.8 for GPU acceleration, Python 3.8 as the primary programming language, and Ubuntu 20.04 LTS as the operating system. The deep learning framework PyTorch 2.0.0 was utilized for model implementation and training, ensuring compatibility with the specified hardware configuration. A complete forward prediction cycle (training and validation) required approximately 9.5 min on this setup. All experiments were performed under this environment to maintain consistency in computational performance and reproducibility.

Reporting summary
Further information on research design is available in the Nature Portfolio Reporting Summary linked to this article.

Data availability
All data supporting the findings of this study are available within the article and its Supplementary Information. Source data are provided with this paper. And the data are also available at https://doi.org/10.5281/zenodo.15261721[50]. Source data are provided with this paper.

Code availability
The code supporting this study are available at GitHub https://github.com/Zhangyh1432/CPP_Customize_Transfer_Learning/tree/main and Zenodo https://doi.org/10.5281/zenodo.15208293[51], which includes all experimental steps, model implementations, and a detailed runtime guide to ensure reproducibility.

References

1. Liu, J. et al. Circularly polarized organic ultralong room-temperature phosphorescence: generation, enhancement, and application. *Adv. Funct. Mater.* **34**, 2414086 (2024).
2. Ma, S. et al. Intense circularly polarized fluorescence and room-temperature phosphorescence in carbon dots/chiral helical polymer composite films. *ACS Nano* **17**, 6912–6921 (2023).
3. Liu, Q. et al. Circularly polarized room temperature phosphorescence through twisting-induced helical structures from polyvinyl alcohol-based fibers containing hydrogen-bonded dyes. *Angew. Chem. Int. Ed.* **63**, e202403391 (2024).
4. MacKenzie, L. E. & Pal, R. Circularly polarized lanthanide luminescence for advanced security inks. *Nat. Rev. Chem.* **5**, 109–124 (2020).
5. Liu, D. et al. Highly efficient circularly polarized near-infrared phosphorescence in both solution and aggregate. *Nat. Photonics* **18**, 1276–1284 (2024).
6. Furlan, F. et al. Chiral materials and mechanisms for circularly polarized light-emitting diodes. *Nat. Photonics* **18**, 658–668 (2024).
7. Hao, W. C., Li, Y. G. & Liu, M. H. Endowing phosphor materials with long-afterglow circularly polarized phosphorescence via ball milling. *Adv. Opt. Mater.* **9**, 2100452 (2021).
8. Liang, X. et al. Organic room-temperature phosphorescence with strong circularly polarized luminescence based on para-cyclophanes. *Angew. Chem. Int. Ed.* **58**, 17220–17225 (2019).
9. Garain, S., Sarkar, S., Garain, B. C., Pati, S. K. & George, S. J. Chiral arylene diimide phosphors: circularly polarized ambient phosphorescence from bischromophoric pyromellitic diimides. *Angew. Chem. Int. Ed.* **61**, e202115773 (2022).
10. Jiang, Y. T. et al. Chiral-guest induced multicolor-tunable circularly polarized room temperature phosphorescence. *Adv. Opt. Mater.* **12**, 2302482 (2024).
11. He, M., Ding, C., Guo, H. & Li, Q. Room temperature phosphorescence materials based on small organic molecules: Design strategies and applications. *Responsive Mater.* **2**, e20240014 (2024).
12. Xu, M. C. et al. Designing hybrid chiral photonic films with circularly polarized room-temperature phosphorescence. *ACS Nano* **14**, 11130–11139 (2020).
13. Cao, M. N. et al. Biobased and biodegradable films exhibiting circularly polarized room temperature phosphorescence. *Nat. Commun.* **15**, 2375 (2024).
14. Huang, Z., He, Z., Ding, B., Tian, H. & Ma, X. Photoprogrammable circularly polarized phosphorescence switching of chiral helical polyacetylene thin films. *Nat. Commun.* **13**, 7841 (2022).
15. Wang, X. J., Ma, S., Zhao, B. & Deng, J. P. Frontiers in circularly polarized phosphorescent materials. *Adv. Funct. Mater.* **33**, 2214364 (2023).
16. Li, H. et al. Single-component color-tunable circularly polarized organic afterglow through chiral clusterization. *Nat. Commun.* **13**, 429 (2022).
17. Jiang, K. D., Fan, Q. Y., Guo, D. K., Song, C. F. & Guo, J. B. Circularly polarized room-temperature phosphorescence with an ultrahigh dissymmetry factor from carbonized polymer dots by stacked chiral photonic films. *ACS Appl. Mater. Interfaces* **15**, 26037–26046 (2023).
18. Wang, X. J., Zhao, B. & Deng, J. P. Liquid crystals doped with chiral fluorescent polymer: multi-color circularly polarized fluorescence and room-temperature phosphorescence with high dissymmetry factor and anti-counterfeiting application. *Adv. Mater.* **35**, 2304405 (2023).
19. Liu, J. et al. Circularly polarized organic ultralong room-temperature phosphorescence with a high dissymmetry factor in chiral helical superstructures. *Adv. Mater.* **36**, 2305834 (2024).
20. Xu, L. et al. Crystallization-driven asymmetric helical assembly of conjugated block copolymers and the aggregation induced white-light emission and circularly polarized luminescence. *Angew. Chem. Int. Ed.* **59**, 16675–16682 (2020).
21. Kang, W. et al. A photo- and thermo-driven azoarene-based circularly polarized luminescence molecular switch in a liquid crystal host. *Angew. Chem. Int. Ed.* **62**, e202311486 (2023).
22. Liu, J. et al. Circularly polarized luminescence in chiral orientationally ordered soft matter systems. *Responsive Mater.* **1**, e20230005 (2023).
23. Yang, D. et al. Steering triplet–triplet annihilation upconversion through enantioselective self-assembly in a supramolecular gel. *J. Am. Chem. Soc.* **143**, 13259–13265 (2021).
24. Zhang, G., Cheng, X., Wang, Y. & Zhang, W. Supramolecular chiral polymeric aggregates: Construction and applications. *Aggregate* **4**, e262 (2022).
25. Lv, J. W. et al. Gold nanowire chiral ultrathin films with ultrastrong and broadband optical activity. *Angew. Chem. Int. Ed.* **56**, 5055–5060 (2017).
26. Probst, P. T. et al. Mechano-tunable chiral metasurfaces via colloidal assembly. *Nat. Mater.* **20**, 1024–1028 (2021).
27. Park, J. M., Cao, Y., Watanabe, K., Taniguchi, T. & Jarillo-Herrero, P. Tunable strongly coupled superconductivity in magic-angle twisted trilayer graphene. *Nature* **590**, 249–255 (2021).
28. Lv, J. et al. Self-assembled inorganic chiral superstructures. *Nat. Rev. Chem.* **6**, 125–145 (2022).
29. Xie, Y. F. et al. Inverse design of chiral functional films by a robotic AI-guided system. *Nat. Commun.* **14**, 6177 (2023).
30. Xie, Y. F. et al. Flexible, Programmable, Chiroptical Polymer Films of Twisted Stacking Layers for Circular Polarization-Based Multiplex Color Display. *Adv. Opt. Mater.* **10**, 2102197 (2022).
31. Zhao, W. J., He, Z. K. & Tang, B. Z. Room-temperature phosphorescence from organic aggregates. *Nat. Rev. Mater.* **5**, 869–885 (2020).
32. Bolton, O., Lee, K., Kim, H.-J., Lin, K. Y. & Kim, J. Activating efficient phosphorescence from purely organic materials by crystal design. *Nat. Chem.* **3**, 205–210 (2011).
33. An, Z. et al. Stabilizing triplet excited states for ultralong organic phosphorescence. *Nat. Mater.* **14**, 685–690 (2015).
34. Dai, Y. K. et al. Machine-learning-driven G-quartet-based circularly polarized luminescence materials. *Adv. Mater.* **36**, 2310455 (2024).
35. Segler, M. H. S., Preuss, M. & Waller, M. P. Planning chemical syntheses with deep neural networks and symbolic AI. *Nature* **555**, 604–610 (2018).
36. Gómez-Bombarelli, R. et al. Design of efficient molecular organic light-emitting diodes by a high-throughput virtual screening and experimental approach. *Nat. Mater.* **15**, 1120–1127 (2016).
37. Friederich, P., Häse, F., Proppe, J. & Aspuru-Guzik, A. Machine-learned potentials for next-generation matter simulations. *Nat. Mater.* **20**, 750–761 (2021).

38. Lee, J. & Asahi, R. Transfer learning for materials informatics using crystal graph convolutional neural network. *Comput. Mater. Sci.* **190**, 110314 (2021).
39. Li, X. et al. Manifold learning of four-dimensional scanning transmission electron microscopy. *Npj Comput. Mater.* **5**, 5 (2019).
40. Jiang, C. et al. Transfer learning guided discovery of efficient perovskite oxide for alkaline water oxidation. *Nat. Commun.* **15**, 6301 (2024).
41. Xu, P. C., Ji, X. B., Li, M. J. & Lu, W. C. Small data machine learning in materials science. *Npj Comput. Mater.* **9**, 42 (2023).
42. Yamada, H. et al. Predicting materials properties with little data using shotgun transfer learning. *ACS Cent. Sci.* **5**, 1717–1730 (2019).
43. Jablonka, K. M., Schwaller, P., Ortega-Guerrero, A. & Smit, B. Leveraging large language models for predictive chemistry. *Nat. Mach. Intell.* **6**, 161–169 (2024).
44. Bran, A. M. et al. Augmenting large language models with chemistry tools. *Nat. Mach. Intell.* **6**, 525–535 (2024.
45. Boiko, D. A., MacKnight, R., Kline, B. & Gomes, G. Autonomous chemical research with large language models. *Nature* **624**, 570–578 (2023).
46. Bao, Y. J., Wen, L., Chen, Q., Qiu, C. W. & Li, B. J. Toward the capacity limit of 2D planar Jones matrix with a single-layer metasurface. *Sci. Adv.* **7**, eabh0365 (2021).
47. Zhang, Y. F. et al. Large-area, flexible, transparent, and long-lived polymer-based phosphorescence films. *J. Am. Chem. Soc.* **143**, 13675–13685 (2021).
48. Wang, D. L. et al. Achieving color-tunable and time-dependent organic long persistent luminescence via phosphorescence energy transfer for advanced anti-counterfeiting. *Adv. Funct. Mater.* **33**, 2208895 (2023).
49. Li, D., Yang, J., Fang, M. M., Tang, B. Z. & Li, Z. Stimulus-responsive room temperature phosphorescence materials with full-color tunability from pure organic amorphous polymers. *Sci. Adv.* **8**, eabl8392 (2022).
50. Liu X. Design of Circularly Polarized Phosphorescence Materials Guided by Transfer Learning.Design_of_cpp_materials_guided_by_transfer_learning:v1, https://doi.org/10.5281/zenodo.15261721 (2025).
51. Zhang, Y. H. Design of Circularly Polarized Phosphorescence Materials Guided by Transfer Learning.Zhangyh1432/CPP_Customize_Transfer_Learning:v1, https://doi.org/10.5281/zenodo.15208293 (2025).

Acknowledgements

This research was carried out with funds received from the Strategic Priority Research Program of the Chinese Academy of Sciences (XDB0450302), the National Natural Science Foundation of China (22071233, 52373122), The Young Scientists Fund of the National Natural Science Foundation of China (GG2060200182), China Postdoctoral Science Foundation (BH2060000242), Youth Project of the Provincial Natural Science Foundation of Anhui (2408085QB041), Fundamental Research Funds for the Central Universities (WK2060000071) and AnHui Estone Materials Technology Co., Ltd. This work was partially carried out at the University of Science and Technology of China's Center for Micro and Nanoscale Research and Fabrication and the Instruments Center for Physical Science, University of Science and Technology of China.

Author contributions

G.Z., J.J. and W.S. were responsible for the overall project design, direction and supervision. X.L. and Y.X. conducted the synthesis and characterization of all samples. Y.Z. carried out the construction and development of the forward prediction model and the reverse design model. L.W. built the large language models with the help of L.C. L.G. performed the CD measurements and analysis. J.L. (JH.L.), and J.L. (JL.L.) contributed to the preparation of DBCz/PVA. H.Z. contributed to g_{lum} measurements and analysis. All authors contributed to the discussion of results and paper writing.

Competing interests

The authors declare no competing interests.

Additional information

Supplementary information The online version contains supplementary material available at https://doi.org/10.1038/s41467-025-60310-6.

Correspondence and requests for materials should be addressed to Weiwei Shang, Jun Jiang or Gang Zou.

Peer review information *Nature Communications* thanks Guillaume Godin and the other, anonymous, reviewer(s) for their contribution to the peer review of this work. A peer review file is available.

Reprints and permissions information is available at http://www.nature.com/reprints

Publisher's note Springer Nature remains neutral with regard to jurisdictional claims in published maps and institutional affiliations.

Open Access This article is licensed under a Creative Commons Attribution-NonCommercial-NoDerivatives 4.0 International License, which permits any non-commercial use, sharing, distribution and reproduction in any medium or format, as long as you give appropriate credit to the original author(s) and the source, provide a link to the Creative Commons licence, and indicate if you modified the licensed material. You do not have permission under this licence to share adapted material derived from this article or parts of it. The images or other third party material in this article are included in the article's Creative Commons licence, unless indicated otherwise in a credit line to the material. If material is not included in the article's Creative Commons licence and your intended use is not permitted by statutory regulation or exceeds the permitted use, you will need to obtain permission directly from the copyright holder. To view a copy of this licence, visit http://creativecommons.org/licenses/by-nc-nd/4.0/.

© The Author(s) 2025